



HAL
open science

Viscous dissipation in the collision between a sphere and a textured wall

Anne Mongruel, Philippe Gondret

► **To cite this version:**

Anne Mongruel, Philippe Gondret. Viscous dissipation in the collision between a sphere and a textured wall. *Journal of Fluid Mechanics*, 2020, 896, pp.A8. 10.1017/jfm.2020.325 . hal-03896883

HAL Id: hal-03896883

<https://hal.science/hal-03896883v1>

Submitted on 26 Jun 2023

HAL is a multi-disciplinary open access archive for the deposit and dissemination of scientific research documents, whether they are published or not. The documents may come from teaching and research institutions in France or abroad, or from public or private research centers.

L'archive ouverte pluridisciplinaire **HAL**, est destinée au dépôt et à la diffusion de documents scientifiques de niveau recherche, publiés ou non, émanant des établissements d'enseignement et de recherche français ou étrangers, des laboratoires publics ou privés.

Viscous dissipation in the collision between a sphere and a textured wall

Anne Mongruel¹ and Philippe Gondret^{2†}

¹PMMH, CNRS, ESPCI Paris, PSL University, Sorbonne Université, Université de Paris, 75005 Paris, France

²Université Paris-Saclay, CNRS, Laboratoire FAST, 91405, Orsay, France

(Received xx; revised xx; accepted xx)

A model is presented for the bouncing dynamics of a fluid-immersed sphere impacting normally a textured wall with micro-pillars. By taking into account the hydrodynamic and contact interactions between the smooth sphere and the textured wall, the complete motion of the sphere is recovered when approaching, colliding with and bouncing off the wall. We demonstrate that the critical Stokes number for the bouncing transition, St_c is the sum of two contributions corresponding to dissipation prior and during the collision, both contributions being critically influenced by the geometrical parameters of the model roughness. The experimental data obtained from interferometric measurements are found in agreement with the theoretical predictions. In the bouncing regime, the coefficient of restitution is also derived analytically and shows a linear evolution with the Stokes number St just above the bouncing transition, in agreement with the experimental data obtained very close to St_c .

1. Introduction

Collisions of particles in fluids occur in many natural flows and industrial processes such as sediment transport or fluidized beds. These collisions are important in the complex flow dynamics displayed by dispersed media, as for the different regimes of sediment transport (bed load, saltation, suspension load) or of gravity driven avalanches (dense or aerosol regimes, debris flows). The coefficient of restitution of the collision, corresponding to the ratio of the rebound velocity to the impact velocity is a key parameter characterizing the collision process. For dry collisions, some dissipation may arise from different mechanisms making the coefficient of restitution to be smaller than the value one corresponding to an idealized elastic Hertz contact [Johnson (1985)]. These different mechanisms are namely the viscoelasticity and plasticity of materials, and the excitation of vibrational modes as shown, e.g. by Falcon *et al.* (1998), Ruiz-Angelo, Roshankhah & Hunt (2019) and King *et al.* (2018), respectively. For wet collisions, however, the interstitial fluid plays a major role in the dissipation. Dealing with the complex elasto-hydrodynamic process of particle collisions in fluids, Davis, Serayssol & Hinch (1986) introduced two dimensionless parameters: the Stokes number St , ratio of the particle inertia relative to viscous forces, and an elasticity parameter ϵ , ratio of viscous to elastic forces. In this first theoretical approach and the following works of Lian, Adams & Thornton (1996) considering a simplified Hertzian-like profile of the elastic spheres and of Marshall (2011) considering the corner flow associated to the varying contact region, idealized smooth particles are made to rebound from a lubrication film. In these elasto-hydrodynamic models, bouncing occurs without solid contact, due to particle deformation induced by the high lubrication

† Email address for correspondence: philippe.gondret@universite-paris-saclay.fr

pressure that arises between closely approaching smooth surfaces. The coefficient of restitution depends namely on the Stokes number, with a zero value corresponding to no bouncing below some critical value St_c and an increasing value with St above St_c . In the experiments of Barnocky & Davis (1988), the observations of dry spheres falling in the air onto a target wall covered by a thin layer of viscous liquid validated the importance of the Stokes number for wet collisions of particles. Using fast video cameras, Joseph *et al.* (2001) and Gondret, Lance & Petit (2002) measured the coefficient of restitution of liquid-immersed particles: a critical number $St_c \simeq 10$ was found for the bouncing transition and the coefficient of restitution increases with the Stokes number from zero to an asymptotic value corresponding to dry collision. However, the surface roughness was also shown by Joseph *et al.* (2001) to lead to significant dispersion in the results. Surface roughness is an important parameter as it regularizes the divergence of the lubrication force when the sphere/wall gap vanishes and lead to a solid contact in a finite time: Smart & Leighton (1989) showed that the measurement of the settling time for sphere in initial solid contact with a wall gives access to a so-called “hydrodynamic surface roughness”. Computations for a two-dimensional wedge made by Cawthorn & Balmforth (2010) together with lubrication theory and an approximate analytical solution all predict a logarithmic divergence of the force with the minimum separation, which leads to the conclusion that an object falling vertically under gravity will therefore make contact with an underlying plane surface in finite time if roughened by asperities with sharp corners. The influence of surface roughness on the sphere/wall hydrodynamic interaction was considered theoretically by Yang & Hunt (2008) and numerically by Ardekani & Rangel (2008), Simeonov & Calantoni (2012), Izard, Bonometti & Lacaze (2014) and Costa *et al.* (2015). The question of the solid-on-solid contact in the sphere-wall collision in a viscous fluid was investigated recently by Birwa *et al.* (2018) using an electrical experimental set-up: a voltage was applied between the plate and the sphere, and when the sphere makes or breaks electrical contact with the plate, the circuit closes or opens. Birwa *et al.* (2018) have observed that the ball makes direct mechanical contact with the plate during the bounce, in contrast to expectations based on elasto-hydrodynamic theory. The solid-on-solid contact occurs even just below the threshold of bouncing characterized by the critical Stokes number value $St_c \simeq 6$. Birwa *et al.* (2018) conclude that the mechanical contact between two colliding liquid-immersed objects is generic and will occur for any realistic surface roughness.

To investigate experimentally the influence of a surface roughness on the approach and bouncing dynamics of a sphere in a liquid, Chastel (2015) used an interferometric technique providing high resolution in time and space. The technique is based on a metallic sphere settling in a viscous fluid, that acts as a moving mirror reflecting a laser beam. Interference fringes are formed that move according to the sphere motion, the later is thus measured with a spatial resolution of about $0.2 \mu\text{m}$. This settling sphere interferometer was first developed by Lecoq *et al.* (1993) and later used by Lecoq *et al.* (2004) for measuring the dynamics of a sphere settling towards a corrugated wall at vanishing Reynolds number. With the same technique the dynamics of a sphere was investigated subsequently when approaching a smooth surface at finite Reynolds number [Mongruel *et al.* (2010)], a wall covered with micro-pillars at vanishing Reynolds number [Chastel & Mongruel (2016)] and at finite Stokes number below the bouncing transition [Chastel & Mongruel (2019)]. In the bouncing regime, Chastel, Gondret & Mongruel (2016) recorded the sphere/wall collision dynamics onto micro-textured walls with a time resolution of $2 \mu\text{s}$, and developed an elastic contact model between sphere and micro-pillars. The contact force derived by Chastel, Gondret & Mongruel (2016) is a generalization of the elastic foundation model of Johnson (1985) and leads to analytical

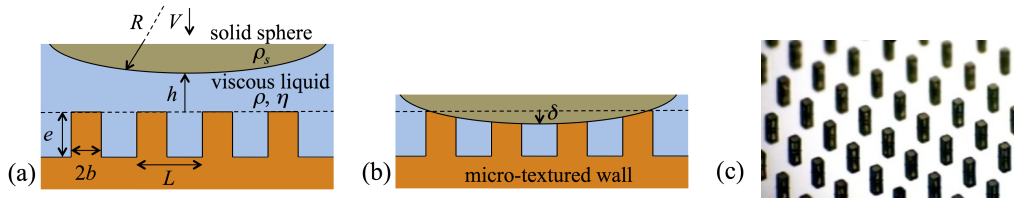


FIGURE 1. (a) Sketch of the studied sphere/wall configuration when the sphere is approaching the textured wall and (b) when the sphere is in contact with the wall. (c) Image of a typical textured wall.

predictions for the penetration depth and the time of collision of the sphere onto the textured wall, with scalings slightly different from the classical Hertz scalings. The measurements of both the sphere penetration depth and time of collision on the textured wall from the high spatial and time resolution of the interferometric technique have been found in good agreement with the theoretical scalings. However, as the fluid dissipation during the collision was not taken into account in the elastic model, the penetration depth was slightly overestimated and the collision time slightly underestimated.

In the present paper, we extend the latter model by taking into account the peculiar viscous dissipation arising during the sphere collision with the micro-pillars and compare to our experimental data. In section 2, we analyse the hydrodynamic and contact interactions between a sphere and a wall covered by a regular array of micro-pillars, and we derive the equations describing the whole collision process: the approach, the collision and the subsequent bouncing of the sphere. The analysis of the results demonstrates that the elasto-hydrodynamic deformation of the pillars is negligible so that solid contact occurs between the sphere and the pillars. In section 3, we derive an expression for the critical Stokes number taking into account the sphere/wall configuration, with two contributions arising from the dissipation prior and during the collision. The influence on this critical Stokes number of the geometrical parameters of the wall texture, that can be considered as a model wall roughness, is then discussed. In section 4, the dependence of the coefficient of restitution with the Stokes number is then derived and compared with the experimental data. We finally conclude in section 5.

2. Bouncing dynamics of a sphere on a textured wall in a surrounding fluid

The configuration studied here is sketched in figure 1: a solid sphere of radius R and density ρ_s is normally driven by gravity towards a micro-textured wall in a viscous liquid of density ρ and dynamic viscosity η . The texture is made of a regular array of vertical pillars of height e , width $2b$, and periodic spacing L , with thus the surface density $\phi = (2b/L)^2$. The sphere position is defined as the distance from the top of the pillars to the bottom of the sphere. This distance is denoted $h > 0$ when the sphere is not touching the pillars (figure 1a) and $\delta > 0$ ($\delta = -h$) when the sphere is in contact with the pillars (figure 1b). The different spheres and micro-pillars used in the experiments of Chastel, Gondret & Mongruel (2016), referred as CGM 2016 in the following, are summarized in table I with the values of the density ratio ρ_s/ρ , the diameter $2R$, the Archimedian number Ar , the surface density ϕ , the height and the width $2b$ of the square pillars. The aspect ratio of the pillars lies in the range $0.5 \lesssim e/2b \lesssim 2.3$. The fluid is a silicon oil (Rhodorsil 47V1000) of density $\rho = 978 \text{ kg/m}^3$ and kinematic viscosity $\nu = \eta/\rho = 10^{-3} \text{ m}^2/\text{s}$. The texture is completely wetted by the oil. The roughness ξ of the sphere surface and of the pillar surface is smaller than $0.1 \text{ }\mu\text{m}$, thus negligibly

ρ_s/ρ	$2R$ (mm)	Ar	ϕ	e (μm)	$2b$ (μm)	Data symbol
7.97	[10.5, 15.9]	[9.9, 34.3]	0.05	[21, 130]	56	●
7.97	[14, 15.9]	[23.5, 34.3]	0.15	[60, 117]	[55, 60]	▲
7.97	[15, 15.9]	[29.9, 34.3]	0.30	[57, 121]	[102, 106]	■
15.95	8	9.4	0.05	[57, 130]	56	▼
15.95	8	9.4	0.15	[60, 117]	[55, 60]	◆

TABLE 1. Parameters values for the different experimental sphere/microtexture configurations of Chastel, Gondret & Mongruel (2016), and data symbols used in figures 6a, 8, and 10.

small compared to the height e and the width $2b$ of the pillars ($\xi \ll e, 2b$). In addition, the geometrical sizes of the textures, e , $2b$ and L are much smaller than the radius of the sphere ($e, 2b, L \ll R$). The pillars have an elastic modulus $E = 1.4$ GPa much smaller than the one of the sphere, so that the sphere may be considered as rigid. The range of the Archimedian number $Ar = \rho(\rho_s - \rho)gR^3/\eta^2$ is between 9.4 and 34.3. As $Ar = (9/4)Re_{St}$ where $Re_{St} = \rho V_{St}(2R)/\eta$ is the Reynolds number based on the Stokes velocity $V_{St} = 2(\rho_s - \rho)gR^2/(9\eta)$ corresponding to the settling velocity of a sphere in an infinite fluid at low Reynolds number, the values of Ar larger than 9/4 in Table 1 mean that fluid inertia plays a non negligible role in these experiments. The sphere is initially maintained at rest by a magnet at the top wall of the cell located at the distance $H = 40.8$ mm above the bottom wall, and released with a zero velocity. The release distance $h_0 = H - 2R$ for the sphere bottom thus varies in the range $24.9 \leq h_0 \leq 32.8$ mm depending on the sphere size. With the interferometric technique of spatial resolution $0.2 \mu\text{m}$ and time resolution $2 \mu\text{s}$ used by CGM 2016, the maximum sphere velocity that can be measured is 100 mm/s, which allows us to explore the sphere dynamics below or close above the bouncing transition but not far above.

2.1. Typical experimental $V(t)$, $h(t)$ and $V(h)$ curves

Figure 2 shows typical experimental curves obtained from the interferometric technique described in details in CGM 2016. The instantaneous position $h + \delta_s$ of the sphere, measured from the final rest position $-\delta_s$ on the deformed micro-pillars, and its instantaneous downward velocity $V = -dh/dt$ are plotted as a function of time in figures 2a and 2b for a steel sphere of density $\rho_s = 7800 \text{ kg/m}^3$ and diameter $2R = 14$ mm settling in silicon oil towards a microtextured wall with square pillars of surface fraction $\phi = 0.15$, of height $e = 60 \mu\text{m}$ and width $2b = 57 \mu\text{m}$. In figure 2(c), the instantaneous velocity $V(t)$ is plotted as a function of its instantaneous position $h(t) + \delta_s$. When approaching the textured wall, the sphere velocity V decreases from about 50 mm/s at $25 \mu\text{m}$ from the wall towards zero at a minimal and negative position corresponding to its maximal penetration distance into the pillars $\delta_m \simeq 3.5 \mu\text{m}$ before rebound. The final sphere position corresponds to its rest position on the deformed pillars with a static penetration distance of $\delta_s \simeq 1.1 \mu\text{m}$. In the case of fig. 2, the sphere touches the top of the pillars at $h = 0$ with an impact velocity $V_i \simeq 19$ mm/s. The rebound velocity when the sphere just bounces back off the wall at $h = 0$ is $V_r \simeq -4$ mm/s, leading to the velocity ratio $-V_r/V_i \simeq 0.2$. The later ratio defines the microscopic restitution coefficient of the solid collision taking into account only the dissipation during the sphere-pillar contact. The contact time (corresponding

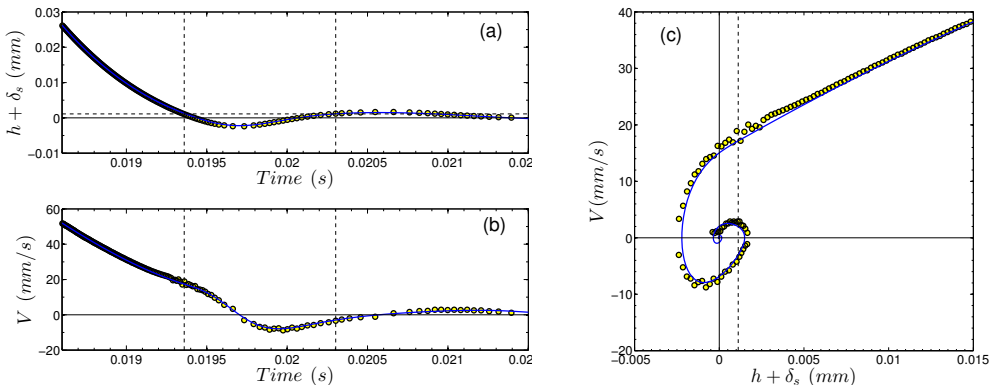


FIGURE 2. (a) Position $h + \delta_s$ of the sphere to the wall relative to its final position $-\delta_s$ and (b) velocity V as a function of time t for a steel sphere of diameter $2R = 14$ mm settling in 47V1000 silicon oil toward an horizontal textured wall with square pillars of surface fraction $\phi = 0.15$, height $e = 60 \mu\text{m}$ and width $2b = 57 \mu\text{m}$, impacting it at the Stokes number $St_i = 0.25$. (c) Instantaneous velocity V of the sphere as a function of its instantaneous position $h + \delta_s$. The (a) horizontal and (c) vertical red dotted lines indicate the position of the top of the underformed textures ($h = 0$) with here $\delta_s = 1.1 \mu\text{m}$. The two vertical dotted lines in (a,b) indicate the times of initial and final solid contact corresponding to the time duration $\tau = 9.6$ ms. The solid curves correspond to model equations (2.1) and (2.3) with $\alpha = 0.9$ and $s = 35 \mu\text{m}$.

to $h \leq 0$) is here $\tau \simeq 0.95$ ms. Note that the sphere bouncing off the wall leads here to a tiny rebound of less than $1 \mu\text{m}$, which means that the present case is very close to the bouncing transition.

2.2. Modeling the sphere motion during the approach phase

When the sphere is near but not touching the wall ($h > 0$), the forces acting on it are the constant driving gravity force $F_g = (4/3)\pi R^3 \rho_s g$ and the fluid forces, which can be decomposed into three parts : (i) the static part corresponding to the constant Archimedian buoyancy force $F_A = -(4/3)\pi R^3 \rho g$ from the static pressure field, (ii) the (quasi-)steady part of the drag force $F_D(t) = -C_{Dw} 6\pi\eta R V(t)$, and (iii) the unsteady part of the drag force corresponding to the added-mass term $F_{am}(t) = -C_{am} (4/3)\pi R^3 \rho dV/dt$. The two last fluid force terms are modified by the near wall as follows.

Concerning the coefficient of the added-mass term, its value $C_{am} = 1/2$ from potential flow theory for an isolated sphere far from any boundary is increased by the near wall. The modified value for a sphere in normal motion relative to a flat wall can be calculated from potential flow theory using images and is given as a series with $C_{am} = 1/2 + 3R/16(R+h)$ at first order [Milne-Thomson (1968)] and with the approximate expression $C_{am} \simeq 1/2 + 0.8(1.9+h/R)^{-3.9}$ values proposed by Ardekani & Rangel (2008) for all h/R . In the present case where the sphere is very close to the wall with vanishing h/R values, this coefficient can be considered as constant with the value $C_{am} \simeq 0.56$, only 12% larger than the usual far value 0.5.

The (quasi-)steady drag force term is also increased by the near wall. For a smooth sphere at vanishing Re number in normal motion close to a smooth solid wall ($h/R \ll 1$), the huge wall-correction factor to the Stokes force $F_{St} = -6\pi R\eta V$ is $C_{Dw} = R/h$, leading to the well-known lubrication drag force $F_D = -6\pi R^2\eta V/h$, that diverges at vanishing h for smooth surfaces. Here, due to the wall textures, the lubrication force is

regularized during the whole dynamics by a characteristic length s , and writes $F_D = -6\pi R^2 \eta V / (h + s)$. Hence, the drag on the sphere at the distance h from the top of the micro-pillars is the same as near an imaginary smooth wall that would be located at a slightly larger distance $h + s$. The characteristic length s is the near-field (valid for $h \ll L$) shift length introduced by Chastel & Mongruel (2019), which depends on the geometrical parameters of the pillar array (e , L and $2b$ or ϕ), as reported and discussed in details in Appendix A. A semi-empirical correlation based on theoretical arguments developed in Seiwert, Clanet & Quéré (2011) and Chastel & Mongruel (2016) gives $s \simeq e(1 - \phi)[1 + \beta(\phi)(e/L)^2]^{-1/3}$, where the coefficient β , which can be estimated from the work of Kuwabara (1959), varies from about 14 to 90 for ϕ varying from 0.05 to 0.30. This shift length s , which can be seen as an effective hydrodynamic roughness, varies between 17 and 71 μm in the experiments considered here. It is thus much smaller than the size of the sphere but much larger than its surface roughness.

In the case of finite Reynolds number, Mongruel *et al.* (2010) have observed that the sphere velocity varies linearly with the distance h as $V = V_0 h / R$ in the last regime before contact, but with a typical velocity V_0 slightly larger from V_{St} . Hence, an additional numerical prefactor $\alpha = V_{St} / V_0$ slightly smaller than one is needed to fit the experimental data. The coefficient α measured for spheres approaching a smooth surface varies typically between 0.95 and 0.85 with an average value 0.9 for the experiments considered here. This prefactor may reflect some complex unsteady effect such as the integral history force.

The sphere motion can thus be modeled by the equation

$$\frac{4}{3}\pi R^3(\rho_s + C_{am}\rho)\frac{dV}{dt} = \frac{4}{3}\pi R^3(\rho_s - \rho)g - \frac{6\pi R^2 \eta \alpha V}{h + s}. \quad (2.1)$$

This equation can be written in a dimensionless form with the sphere radius R for the length scale, the impact velocity V_i for the velocity scale and the ratio R/V_i for the time scale :

$$\frac{2(\rho_s + C_{am}\rho)RV_i}{9\eta}\frac{d\tilde{V}}{d\tilde{t}} = \frac{V_{St}}{V_i} - \frac{\alpha\tilde{V}}{\tilde{h} + \tilde{s}}, \quad (2.2)$$

where $\tilde{V} = V/V_i$, $\tilde{h} = h/R$, $\tilde{s} = s/R$ and $\tilde{t} = tV_i/R$. Two dimensionless numbers appear in this dimensionless equation: the impact Stokes number $St_i = 2(\rho_s + C_{am}\rho)RV_i/9\eta$ based on the impact velocity and taking into account the added mass effect as introduced by Legendre *et al.* (2006), and the velocity ratio $V_{St}/V_i = 4Ar/9Re_i$, where $Re_i = \rho V_i(2R)/\eta$ is the Reynolds number based on the impact velocity V_i . Following Izard, Bonometti & Lacaze (2014), the three dimensionless numbers that governs the approach dynamics of the sphere towards the micro-textured wall numbers can be either the *a priori* known Ar and density ratio ρ_s/ρ or the *a posteriori* known St_i and Re_i , together with the dimensionless shift length s/R that characterizes here the hydrodynamic effect of the micro-pillars. The consequences of the shift length s are a finite pressure and drag force, and a non-zero velocity for the sphere at $h = 0$. An estimation of elastic deformation of the wall textures detailed in Appendix B gives very small deformation, typically between 0.001 and 0.1 μm , which is smaller or of the order of the microscopic roughness of the sphere surface and texture surface. In the present modeling, we thus do not consider any pillar deformation when $h > 0$ and consider that solid contact occurs at $h = 0$.

2.3. Modeling the sphere motion during the contact phase

When $h \leq 0$, the sphere is thus considered to be in solid contact with the textured wall. For a wall covered by an array of micro-pillars, CGM 2016 has derived a contact model by considering that the pillars behave as independent springs. The non-linear contact force is $F_w = -\pi\phi ER\delta^2/e$, where $\delta = -h$ corresponds now to the wall deformation, with a power exponent 2 for δ , which is different from the exponent 3/2 for the classical Hertz force valid for a sphere in contact with a smooth elastic half-plane. This contact force, validated experimentally by CGM 2016 and then by Maruoka (2019), has been derived under different assumptions : (i) an elastic response of the pillars, (ii) a quasi-static deformation, and (iii) a contact area embedding several pillars. In the set of experiments considered here, these assumptions are satisfied : (i) the relative deformation δ_m/e of the pillars remains smaller than 10^{-1} , thus in the elastic regime. (ii) The solid collision time $\tau \simeq 1$ ms remains much larger than the propagation time of the deformation in the pillars $e/c \simeq 0.1 \mu\text{s}$ where $c = (E/\rho_w)^{1/2} \simeq 10^3$ m/s is the sound velocity in the pillars. Following the criterion $(V_i/c)^{3/5} \ll 1$ expressed by Hunter (1957) in terms of a velocity ratio rather than of a time ratio for the Hertz collision of a sphere onto a smooth wall, the present quasi-static criterion, which is satisfied for the present sphere collision onto the textured wall, can be expressed as $(V_i\phi\rho_w e^2/c\rho_s R^2)^{1/3} \ll 1$. (iii) The number of pillars embedded in the solid collision within the contact disk area of radius $(2R\delta_m)^{1/2}$, and which can be thus estimated as $N \simeq 2\pi R\delta_m/L^2$, is in the range $3 \lesssim N \lesssim 37$. The contact force derived by CGM 2016 is a generalization of the elastic foundation model of Johnson (1985) for solid fraction $\phi \neq 1$, but it would not be valid at the opposite limit of vanishing ϕ where only one pillar would be embedded in the contact [Ledezma-Alonso *et al.* (2016)]. Assuming that the added-mass force and the drag force discussed in section 2.2 remain unchanged during contact, the sphere motion can thus be modeled by the equation

$$\frac{4}{3}\pi R^3(\rho_s + C_{am}\rho) \frac{dV}{dt} = \frac{4}{3}\pi R^3(\rho_s - \rho)g - \frac{6\pi R^2\eta\alpha V}{s - \delta} - \frac{\pi\phi ER\delta^2}{e}. \quad (2.3)$$

This equation governs the sphere motion when $h \leq 0$ during the supposed contact with the pillars until the solid contact breaks with a non zero rebound velocity $-V_r$ at $h = 0$, or until the sphere stops (with $V = 0$ and $dV/dt = 0$) at its final resting position $\delta_s/R = [4e(\rho_s - \rho)g/3\phi E]^{1/2}$, resulting from the balance of apparent weight and elastic contact force. The corresponding dimensionless equation writes

$$St_i \frac{d\tilde{V}}{dt} = \frac{4Ar}{9Re_i} - \frac{\alpha\tilde{V}}{\tilde{s} - \tilde{\delta}} - \frac{\phi ER^2}{6e\eta V_i} \tilde{\delta}^2, \quad (2.4)$$

where $\tilde{\delta} = \delta/R$. Three main dimensionless numbers appear in this dimensionless equation: the impact Stokes number St_i , a gravito-viscous number corresponding here to the velocity ratio $V_{St}/V_i = 4Ar/9Re_i$, and an elasto-viscous parameter $\phi ER^2/6e\eta V_i$. The later parameter corresponds to the inverse of the elastic parameter introduced by Davis, Serayssol & Hinch (1986) for the collision of an elastic sphere onto a smooth wall but is somewhat different here due to the micro-pillars. Note that this elastic parameter is very large as the dimensionless deformation $\tilde{\delta}$ remains very small.

2.4. Comparison between model and experiments

Let us now compare the data with the modeling. The curves obtained by numerical integration of the model eqs. (2.1) and (2.3) are very close to the data points of figure

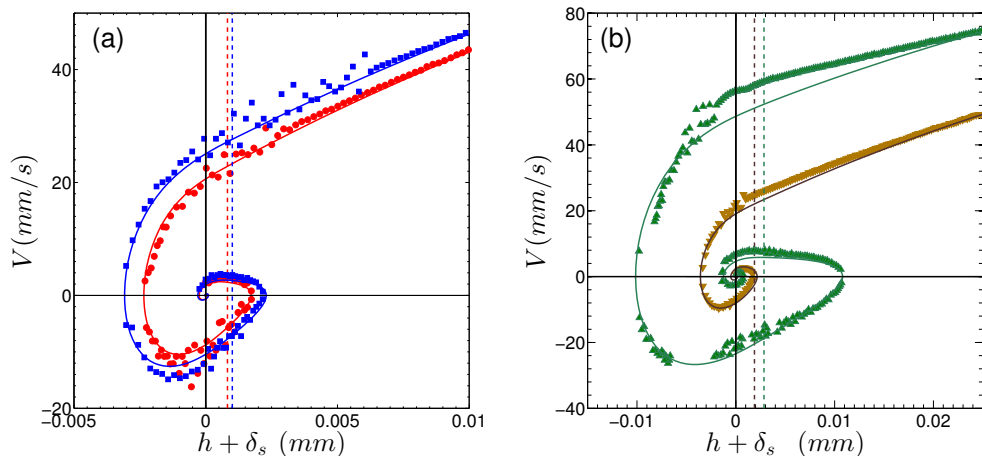


FIGURE 3. Instantaneous velocity V as a function of the instantaneous position $h + \delta_s$ relative to its final static position $-\delta_s$ for a steel sphere of diameter (a) $2R = 15$ mm impacting a textured wall with micro-pillars of surface fraction $\phi = 0.30$, height $e = 57 \mu\text{m}$ and width $2b = 102 \mu\text{m}$ (\bullet) or $e = 85 \mu\text{m}$ and $2b = 106 \mu\text{m}$ (\blacksquare), and for (b) $2R = 14$ mm, $\phi = 0.05$, $2b = 56 \mu\text{m}$, and $e = 57 \mu\text{m}$ (∇) or $e = 130 \mu\text{m}$ (\triangle). Model equations (2.1) and (2.3) with $\alpha = 0.9$ and with (a) $s = 24.5 \mu\text{m}$ ($-$) or $s = 26.5 \mu\text{m}$ ($-$), and (b) $s = 43 \mu\text{m}$ ($-$) or $s = 57 \mu\text{m}$ ($-$).

2 all along the sphere motion, not only in the approach phase before the wall impact but also during the contact and the subsequent bouncing. In particular, the penetration distance δ_m and the bouncing height are remarkably well predicted. The dimensionless number values for this case are $St_i \simeq 0.25$, $V_{St}/V_i = 4Ar/9Re_i \simeq 39$, and $\phi ER^2/6e\eta V_i \simeq 1.54 \times 10^9$. Note that the two corrections for the drag force used here are not fitting parameters, but the near-field shift length $s \simeq 35 \mu\text{m}$ ($\bar{s} \simeq 5 \times 10^{-3}$) and the factor $\alpha \simeq 0.9$, obtained from previous experiments at small Reynolds number near the same micro-pillars (Chastel & Mongruel 2019) and at finite Reynolds number near a smooth wall (Mongruel *et al.* 2010), respectively. This shift length, which is smaller than but of the order of the pillar height, $s/e \simeq 0.58$, corresponds to the effective hydrodynamic roughness of the wall. Taking into account the drag force when the sphere is in solid contact with the wall is crucial for modeling correctly the bouncing dynamics : ignoring the drag force would indeed lead to a significant overestimation of the pillar deformation (4.4 instead of $3.5 \mu\text{m}$), and then a large overestimation of the subsequent rebound velocity (-17 instead of -4 mm/s) and of the bouncing height in the fluid (5 instead of $0.5 \mu\text{m}$). The very good agreement that is observed between modeling and experimental data when taking into account all the terms in eqs. (2.1) and (2.3) is also observed for many other cases, examples of which are depicted in figure 3 and figure 4 for the bouncing motion of a steel sphere and a tungsten carbide sphere respectively, on pillar arrays of various geometries.

Figure 3(a) shows two typical $V(h)$ curves for a steel sphere of diameter $2R = 15$ mm colliding with a wall with micro-pillars of surface fraction ($\phi = 0.30$) and of two different heights ($e = 57$ and $85 \mu\text{m}$) with about the same width ($2b \simeq 100 \mu\text{m}$). As expected, the impact velocity is slightly larger for higher pillars : $V_i \simeq 27$ mm/s corresponding to an impact Stokes number $St_i \simeq 0.39$ for $e = 85 \mu\text{m}$ when compared to $V_i \simeq 23$ mm/s ($St_i \simeq 0.33$) for $e = 57 \mu\text{m}$. The modeling uses a correction factor $\alpha \simeq 0.9$, and shift lengths $s = 26.5 \mu\text{m}$ and $s = 24.5 \mu\text{m}$ respectively for the higher and lowest pillars. In the two cases, very small rebounds of about 2 and $3 \mu\text{m}$ are observed.

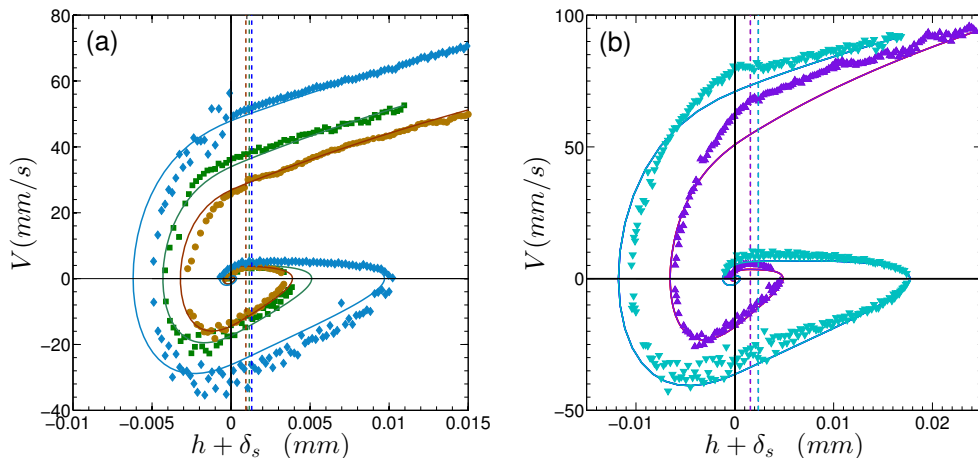


FIGURE 4. Same as fig. 3 for a tungsten carbide sphere ($2R = 8$ mm) towards a textured wall with pillars of (a) surface fraction $\phi = 0.15$ and of height $e = 60$ μm and width $2b = 57$ μm (\bullet), $e = 91$ μm and $2b = 60$ μm (\blacksquare), or $e = 117$ μm and $2b = 55$ μm (\diamond), (b) $\phi = 0.05$, $2b = 56$ μm and $e = 57$ μm (\blacktriangle) or $e = 130$ μm (\blacktriangledown). The two vertical dotted lines stand for the top of the undeformed textures at $h = 0$ in each case. The solid curves corresponds to model equations (2.1) and (2.3) with $\alpha = 0.85$ and with (a) $s = 35$ μm ($-$), $s = 39$ μm ($-$) or $s = 42$ μm ($-$) and (b) $s = 27$ μm ($-$) or $s = 47$ μm ($-$).

Two other typical $V(h)$ curves are shown in figure 3(b) for a steel sphere of diameter $2R = 14$ mm colliding with a wall with micro-pillars of smaller surface fraction ($\phi = 0.05$) and of two different heights ($e = 57$ and 130 μm) with the same width ($2b \simeq 56$ μm). Compared to figure 3(a), the effect of decreasing the pillar surface fraction and increasing the pillar height is seen to amplify the rebound, leading to a larger impact velocity $V_i \simeq 59$ mm/s ($St_i \simeq 0.79$) for $e = 130$ μm . As expected, the static deformation is larger for the higher pillars as the contact force is weaker: $\delta_s \simeq 3$ for $e = 130$ μm compared to 2 μm for $e = 57$ μm . Interestingly, the case $e = 57$ μm for which $V_i \simeq 25$ mm/s ($St_i \simeq 0.33$) corresponds exactly to the bouncing transition as the maximal position of the sphere after the collision is here $h = 0$, i.e. the sphere remains in contact with to the pillars. The case at $St_i \simeq 0.79$ is clearly above the bouncing transition with a bouncing height of about 7 μm . Using the correction factor $\alpha \simeq 0.9$ together with the shift length $s = 57$ μm and $s = 43$ μm for the highest and the lowest pillars, respectively, it can be seen that the modeling does not fit perfectly the approach phase in the case $e = 130$ μm , but performs very well in the contact and rebound phases.

Finally, figure 4a and 4b show various $V(h)$ curves for a tungsten carbide sphere of diameter $2R = 8$ mm approaching a wall with micro-pillars of surface fraction $\phi = 0.15$ and $\phi = 0.05$ respectively, and of different heights e (ranging from 60 to 130 μm) with about the same width $2b$. Again, we observe that for a given pillar surface fraction, increasing the pillar height amplifies the bouncing, with higher impact velocities and hence larger penetration depths and also larger bouncing heights. For instance, at $\phi = 0.15$, $V_i \simeq 38$ mm/s ($St_i \simeq 0.56$) for $e = 91$ μm compared to $V_i \simeq 51$ mm/s ($St_i \simeq 0.76$) for $e = 117$ μm . The same observation can be made when decreasing the pillar surface fraction at a given pillar height: for $e = 57$ μm , $V_i \simeq 30$ mm/s ($St_i \simeq 0.44$) at $\phi = 0.15$ compared to $V_i \simeq 68$ mm/s ($St_i \simeq 1$) at $\phi = 0.05$. The modeling still gives correct results, but it happens to overestimate the bouncing height or the penetration distance in some cases.

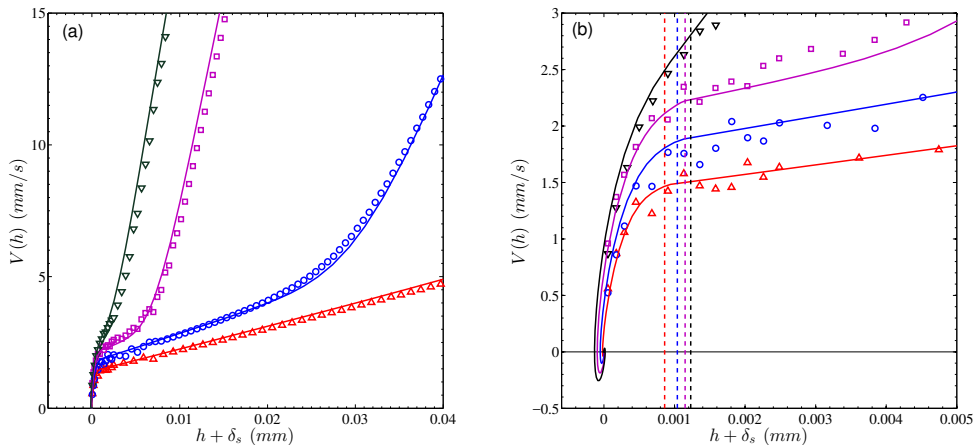


FIGURE 5. (a) Same as fig. 3 for steel spheres of diameter $2R = 10.5$ (\triangle), 12.7 (\circ), 14 (\square), and 15 mm (∇), towards a textured wall with pillars of surface fraction $\phi = 0.05$ and of height $e = 21 \mu\text{m}$ and width $2b = 57 \mu\text{m}$. The solid curves corresponds to model equations (2.1) and (2.3) with $s = 17 \mu\text{m}$ and (a) $\alpha = 0.98$ ($-$), 0.95 ($-$), 0.90 ($-$), 0.90 ($-$). (b) Zoom on figure (a) with vertical dotted lines standing for the top of the undeformed textures at $h = 0$ with $\delta_s = 0.86$ ($- - -$), 1.04 ($- - -$), 1.15 ($- - -$), and $1.23 \mu\text{m}$ ($- - -$).

All the results presented in figures 2, 3 and 4 concern cases where small bouncing of the spheres off the wall is observed thus slightly above the bouncing transition. In some cases, no bouncing of the spheres off the wall is observed as shown in figure 5. In that figure, the experimental measurements of the sphere motion is plotted for four different diameters of steel sphere impacting the same textured wall at a finite but very low velocity. Indeed the impact velocity taken at the top of the underformed structure ($h = 0$) is $V_i \approx 1.4, 1.8, 2.2$, and 2.8 mm/s, corresponding to very low impact Stokes number : $0.014 \lesssim St_i \lesssim 0.04$. The model indeed predicts the “sticking” collision observed experimentally : the spheres come to rest with a strong monotonic decrease of velocity down to their final position $h = -\delta_s$.

3. The critical Stokes number for bouncing

The fact that a sphere approaching a wall will rebound or not off the wall is here related to viscous dissipation. This viscous dissipation arises during the two phases of the sphere motion : (i) the approach towards the textured wall and (ii) the solid contact with the micro-pillars during the collision.

Let us first consider the approach phase. As seen in fig. 5, the apparent weight can be neglected when compared to the large lubrication force near the wall and the sphere is thus strongly decelerated. The balance of sphere inertia (with the added-mass term) and lubrication drag in eq. (2.1) yields a logarithmic variation of the velocity $V(h)$ of the sphere as a function of the distance $h > 0$ [Davis, Serayssol & Hinch (1986)]. With the impact velocity V_i taken as the reference velocity at $h = 0$, one obtains

$$\frac{V(h)}{V_i} \simeq 1 + \frac{\alpha}{St_i} \ln \left(\frac{h+s}{s} \right). \quad (3.1)$$

To obtain an estimate of the velocity V_∞ far from the wall, we extrapolate eq. (3.1) up to the distance $h = R$, at which the lubrication drag force due to the wall becomes of

the order of the Stokes drag force in an infinite fluid ($C_w \simeq 1$). As $R \gg s$ in our case, the estimate $V_\infty = V(h = R)$ of the velocity V_∞ far from the wall is thus given by:

$$\frac{V_\infty}{V_i} \simeq 1 + \frac{\alpha}{St_i} \ln\left(\frac{R}{s}\right). \quad (3.2)$$

Another typical velocity of approach is provided by the terminal settling velocity V_T resulting from the balance of the effective weight of the sphere and the drag force far from the wall. In the present situation where fluid inertia is not negligible, the later drag force is $-6\pi\eta RV(1 + 3Re/16)$, i.e. the Stokes drag modified by the Oseen correction for small fluid inertia (Re is here the Reynolds number based on the velocity V of the sphere). The terminal velocity V_T is thus smaller than the Stokes velocity V_{St} . In the case of figure 2, the terminal settling velocity is $V_T = 376$ mm/s whereas the estimate velocity far from the wall is $V_\infty = 378$ mm/s from equation (3.2) with $V_i \simeq 19$ mm/s ($St_i \simeq 0.25$), $R = 7$ mm, $s \simeq 35 \mu\text{m}$, and $\alpha \simeq 0.9$. In that case, the two velocities V_∞ and V_T are very close to each other. In most cases, V_∞ is slightly smaller than V_T , in the range $0.8V_T \lesssim V_\infty \lesssim V_T$, as the experimental cell is not high enough for the sphere starting from rest at the top of the cell to reach its terminal velocity. We thus choose here to use the characteristic approach velocity V_∞ at the distance R from the wall, to infer a macroscopic Stokes number St from the experimental conditions:

$$St = St_i \frac{V_\infty}{V_i} \simeq St_i + \alpha \ln\left(\frac{R}{s}\right). \quad (3.3)$$

This Stokes number $St = 2(\rho_s + C_{am}\rho)RV_\infty/9\eta$ is close to the one based on the terminal velocity V_T (Legendre *et al.* 2006; Ardekani & Rangel 2008; Izard, Bonometti & Lacaze 2014). In the case of figure 2, this global Stokes number is $St \simeq 4.5$, much larger than the impact Stokes number $St_i \simeq 0.25$.

Let us now estimate the fluid dissipation during the sphere collision with the pillars. During this collision, the contact force on the sphere comes into play and the sphere motion is now given by eq. (2.3). Neglecting the gravity force, the corresponding equation for the energy is given by

$$\frac{2}{3}\pi R^3(\rho_s + C_{am}\rho)V_i^2 = \frac{2}{3}\pi R^3(\rho_s + C_{am}\rho)V(t)^2 + \frac{\pi}{3}\phi E_w \frac{R}{e} \delta(t)^3 - \int_0^\delta \frac{6\pi R^2 \eta \alpha V(t)}{s - \delta} d\delta. \quad (3.4)$$

In this equation, the initial kinetic energy $E_{ki} = (1/2)M_{eff}V_i^2$ of the sphere of effective mass $M_{eff} = (4/3)\pi R^3(\rho_s + C_{am}\rho)$ corresponding to its own mass and the fluid added-mass is partly transferred to the pillars from elastic deformation with the potential energy term $E_p = \int_0^\delta F_w d\delta$ and is partly lost in the fluid flow from viscous dissipation with the term $E_d = \int_0^\delta F_D d\delta$. For a zero fluid dissipation ($\eta = 0$), the sphere motion deduced from this equation would be given by the instantaneous velocity

$$V(t) = V_i \left[1 - \left(\frac{\delta(t)}{\delta_{m0}} \right)^3 \right]^{1/2}, \quad (3.5)$$

where

$$\delta_{m0} = \left(\frac{2\rho_s e R^2 V_i^2}{\phi E} \right)^{1/3} \quad (3.6)$$

would be the corresponding penetration distance as shown by CGM 2016. The energy

dissipation stemming from viscous forces considering this conservative sphere motion would be

$$E_d \simeq 2 \int_0^{\delta_{m0}} \frac{6\pi R^2 \eta \alpha V(t)}{s - \delta} d\delta \simeq 12I\pi R^2 \eta \alpha V_i, \quad (3.7)$$

with

$$I = \int_0^1 \frac{(1 - \hat{\delta}^3)^{1/2}}{\hat{s} - \hat{\delta}} d\hat{\delta}, \quad (3.8)$$

where $\hat{\delta} = \delta/\delta_{m0}$ and $\hat{s} = s/\delta_{m0}$. For large \hat{s} values, this integral term can be approximated by

$$I \simeq \frac{\int_0^1 (1 - \hat{\delta}^3)^{1/2} d\hat{\delta}}{\hat{s}} \simeq \frac{0.84}{\hat{s}}. \quad (3.9)$$

Using the estimate of the fluid dissipation E_d given by eq. 3.7, one can infer a rough estimate of the non bouncing condition for which the initial kinetic energy E_{ki} of the sphere will be dissipated completely. Writing $E_d = E_{ki}$ gives the critical impact velocity, V_{ic} , and hence the following estimation for the critical value St_{ic} of the impact Stokes number :

$$St_{ic} \simeq 4\alpha I, \quad (3.10)$$

where I is the integral term given by eq. (3.8) or approximate eq. (3.9) for large \hat{s} . The predicted evolution for St_{ic} with \hat{s} is shown in figure 6a in the experimental range $2 \lesssim \hat{s} \lesssim 35$. It can be seen that the approximate hyperbolic prediction $St_{ic} \simeq 3/\hat{s}$ (dashed line) is not far from the complete prediction (solid line), with critical impact Stokes number in the range $0.1 \lesssim St_{ic} \lesssim 1.5$. In figure 6a are also plotted all our experimental data where a micro-rebound is observed (filled symbols) or not (open symbols). As our measurements focused on the bouncing transition, most data points corresponding to bouncing are slightly above the theoretical line with only a few data points slightly below. The data corresponding to ‘‘sticking’’ collisions are significantly below the theoretical line, which is quite satisfying.

The estimation for the critical value St_c of the global Stokes number can be written simply as

$$St_c = St_{ic} \frac{V_{\infty c}}{V_{ic}} \simeq \alpha \ln \left(\frac{R}{s} \right) + St_{ic}. \quad (3.11)$$

In the above expression, the critical Stokes number appears as the sum of two terms: a first term arising from the viscous dissipation during the approach phase towards the array of micro-pillars, and a second term arising from viscous dissipation during the contact with the micro-pillars. The first term depends only on the coefficient α and the ratio R/s , thus on the micro-pillar array geometry and on the sphere size. The second term corresponds to the value of St_{ic} discussed above. The theoretical evolution of the critical Stokes number St_c as a function of s/R is shown in figure 6b for $\alpha = 0.9$ and different St_{ic} values from 0 to 1.5. As our experimental measurements focused on the bouncing transition, all our experimental data points are in a narrow range of Stokes number: $3.5 \lesssim St \lesssim 6.5$. The data points for which a ‘‘sticking’’ collision is observed (\times) are all below the solid line which delineates the transition. The other data points for which a (micro-)rebound is observed appear here with different open data symbols depending on the range of St_{ic} . All these data points are fairly observed just around the corresponding theoretical line.

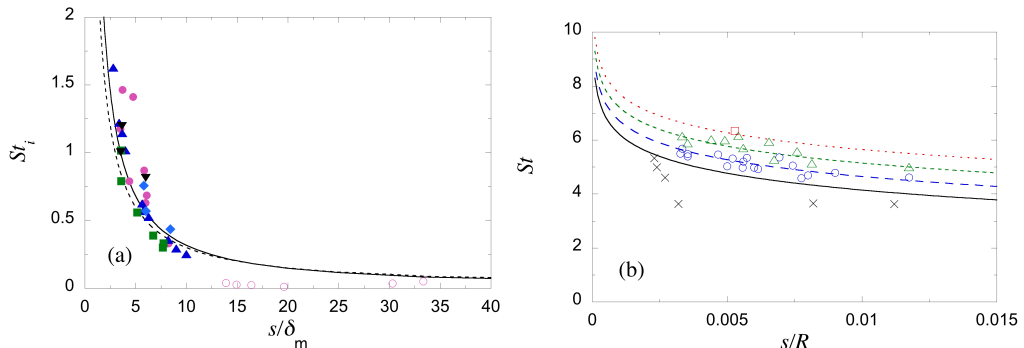


FIGURE 6. (a) Impact Stokes St_i as a function of the ratio $\hat{s} = s/\delta_m$ of the hydrodynamic roughness s relative to the sphere penetration depth δ_m for the experiments (data symbols of table 1) and theoretical predictions $St_{ic} = 4\alpha I$ with $\alpha = 0.9$ and eq. (3.8) for I (—) or eq. (3.9) for I (- - -) at large \hat{s} . Filled symbols correspond to bouncing cases whereas open symbols corresponds to non-bouncing cases. (b) Stokes number St as a function of the hydrodynamic roughness/sphere size ratio s/R for the experiments with open symbols when bouncing is observed for which $0.3 \leq St_{ic} \leq 0.7$ (\circ), $0.8 \leq St_{ic} \leq 1.2$ (\triangle), and $1.3 \leq St_{ic} \leq 1.7$ (\square), and crosses (\times) when no bouncing is observed, together with theoretical prediction $St_c = \alpha \ln(R/s) + St_{ic}$ with $\alpha = 0.9$ and $St_{ic} = 0$ (—), $St_{ic} = 0.5$ (- - -), $St_{ic} = 1$ (- · - ·), and $St_{ic} = 1.5$ (· · ·).

4. The coefficient of restitution for the sphere/wall collision

We have seen that the sphere/wall collision process can be splitted into two parts: (i) the close approach of the sphere towards the micro-pillars and (ii) the subsequent contact of the sphere with the pillars. This second part of the collision can be characterized by the ratio $-V_r/V_i$ of the rebound velocity V_r of the sphere when leaving the solid wall (at $h = 0$) with respect to the impact velocity V_i (at $h = 0$). This ratio $-V_r/V_i$ can be derived considering that the rebound kinetic energy $E_{kr} = (1/2)M_{eff}V_r^2$ is just reduced from the initial kinetic energy E_{ki} by the quantity E_d from viscous dissipation during the collision, as the other force terms are conservative:

$$\frac{-V_r}{V_i} = \left(1 - \frac{E_d}{E_{ki}}\right)^{1/2} \simeq \left(1 - \frac{St_{ic}}{St_i}\right)^{1/2}. \quad (4.1)$$

When $St_i < St_{ic}$, all the kinetic energy of the sphere is dissipated in the fluid during the contact so that no bouncing then occurs and the above expression is not valid. The bouncing and validity of eq. (4.1) requires $St_i > St_{ic}$. For large impact Stokes number ($St_i \gg St_{ic}$), the velocity ratio reduces at first order to $-V_r/V_i = 1 - St_{ic}/2St_i$, whereas it reduces to $-V_r/V_i = (St_i/St_{ic} - 1)^{1/2}$ for small impact Stokes number close to the bouncing/non bouncing critical value St_{ic} ($St_i \simeq St_{ic}$).

Note that the penetration distance is reduced by viscous dissipation. Considering an energy loss of approximately $E_d/2$ with E_d given by eqs (3.7-3.8) corresponding to the first part of the contact from $\delta = 0$ to δ_m , the penetration distance δ_m is given by

$$\frac{\delta_m}{\delta_{m0}} \simeq \left(1 - \frac{St_{ic}}{2St_i}\right)^{1/3}, \quad (4.2)$$

where δ_{m0} is the maximal penetration distance given by eq. (3.6) for a non dissipative collision. Far above the bouncing transition where the dissipation is small ($St_i/St_{ic} \gg 1$), δ_m is only slightly smaller than δ_{m0} , and can be approximated by $\delta_m/\delta_{m0} \simeq 1 - St_{ic}/6St_i$, with, e.g., $\delta_m/\delta_{m0} \simeq 0.98$ at $St_i/St_{ic} = 10$. Closer to the bouncing transition where

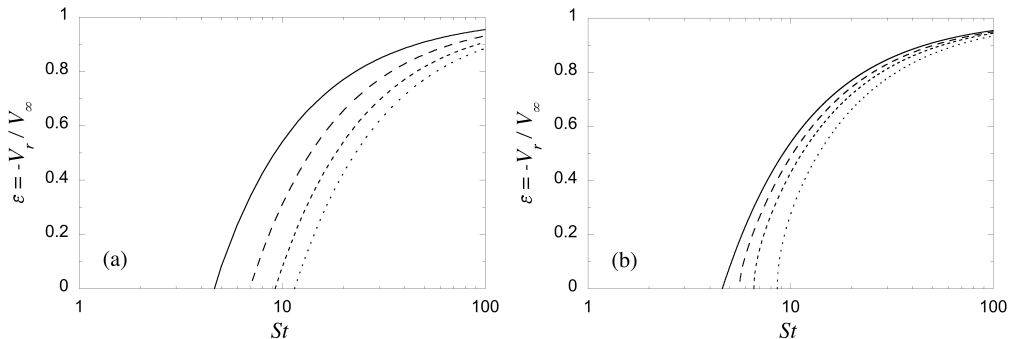


FIGURE 7. (a) Theoretical restitution coefficient of the global collision process $\epsilon = -V_r/V_\infty$ as a function of the global Stokes number St from eq. (4.5) for (a) $St_{ic} = 0$ and $R/s = 10^2$ (—), 10^3 (---), 10^4 (- - -) or 10^5 (···), and (b) for $R/s = 10^2$ and $St_{ic} = 0$ (—), 1 (---), 2 (- - -) or 4 (···).

the dissipation is larger, δ_m is smaller but not so much, as $\delta_m/\delta_{m0} \simeq 2^{-1/3} \simeq 0.8$ at $St_i = St_{ic}$. The experimental penetration distance δ_m reported by CGM 2016 close to the bouncing transition varies between $0.5\delta_{m0}$ and $0.9\delta_{m0}$.

As both the velocity and the penetration distance are reduced by viscous dissipation, the evolution of the collision time is not so intuitive. Following the simple estimation of the typical time of collision $\tau_0 \sim \delta_{m0}/V_i$ for a non dissipative collision with the penetration distance δ_{m0} at the typical velocity V_i , the typical time of collision for a dissipative collision can be estimated as $\tau_v \sim 2\delta_m/(V_i - V_r)$ with the reduced penetration distance δ_m at the typical reduced velocity $(V_i - V_r)/2$. From eq. (4.1) for $-V_r/V_i$ and eq. (4.2) for δ_m , the collision time τ_v for a dissipative collision writes as

$$\frac{\tau_v}{\tau_0} \sim \frac{2 \left(1 - \frac{St_{ic}}{2St_i}\right)^{1/3}}{1 + \left(1 - \frac{St_{ic}}{St_i}\right)^{1/2}}. \quad (4.3)$$

Far above the bouncing transition where the dissipation is small ($St_i/St_{ic} \gg 1$), τ_v can be approximated by $\tau_v/\tau_0 \simeq 1 + St_{ic}/12St_i$, and is thus only slightly larger than τ_0 , e.g., $\tau_v/\tau_0 \simeq 1.01$ at $St_i/St_{ic} = 10$. Closer to the bouncing transition where the dissipation is larger, τ_m is larger but does not diverge: $\tau_v/\tau_0 \simeq 2^{2/3} \simeq 1.6$ at $St_i = St_{ic}$. The experimental collision times τ_v reported by CGM 2016 close to the bouncing transition indeed varies between τ_0 and $1.6\tau_0$. Note that Birwa *et al.* (2018) also found an increase of the contact time for decreasing Stokes number close to their critical value $St_c \simeq 6$: the contact time of a smooth steel sphere colliding onto a smooth steel wall into a viscous silicon oil measured from their electrical set-up was observed to be constant for $1.3 \lesssim St/St_c \lesssim 5$ and increases abruptly very close to St_c ($1 \lesssim St/St_c \lesssim 1.3$) by a factor of about 4 ± 2 .

If we consider the whole collision process embedding not only the sphere/pillars contact but also the previous sphere approach close to the pillars, the global coefficient of restitution corresponds to the ratio $\epsilon = -V_r/V_\infty$ of the rebound velocity V_r to the typical approach velocity V_∞ . With the use of the macroscopic Stokes number $St = St_i V_\infty/V_i$ based on this approach velocity, the global coefficient of restitution is given by

$$\epsilon = \frac{-V_r}{V_i} \frac{V_i}{V_\infty} \simeq \left(1 - \frac{St_{ic}}{St} \frac{V_\infty}{V_i}\right)^{1/2} \frac{V_i}{V_\infty}, \quad (4.4)$$

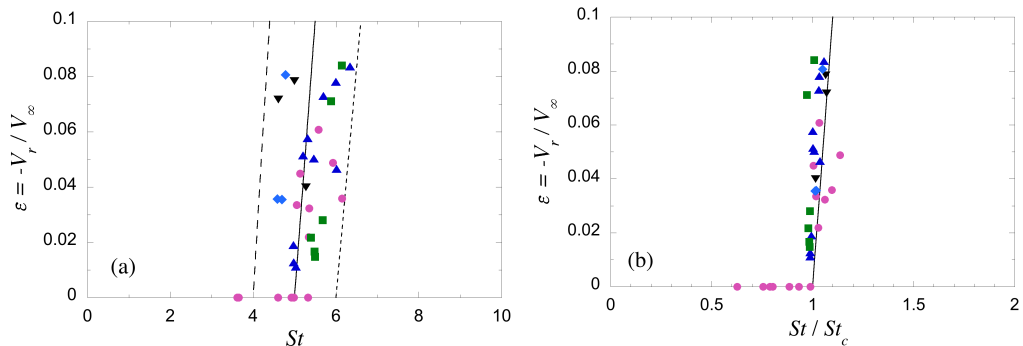


FIGURE 8. Restitution coefficient of the global collision process $\epsilon = -V_r/V_\infty$ (a) as a function of the global Stokes number St with experimental data (data symbols of table 1) and model equation $\epsilon = St/St_c - 1$ for $St_c = 4$ (---), 5 (—) and 6 (-.-), and (b) as a function of the reduced global Stokes number St/St_c .

In eq. (4.4), V_i/V_∞ is the velocity ratio corresponding to the approach phase, and writes from eq. (3.2) :

$$\frac{V_i}{V_\infty} \simeq 1 - \frac{\alpha \ln(R/s)}{St}. \quad (4.5)$$

Finally, the global coefficient of restitution ϵ reduces (for $St \geq St_c$) to

$$\epsilon \simeq \left(1 - \frac{St_{ic}}{St - \alpha \ln(R/s)}\right)^{1/2} \left(1 - \frac{\alpha \ln(R/s)}{St}\right), \quad (4.6)$$

or

$$\epsilon \simeq \left(1 - \frac{St_c}{St}\right)^{1/2} \left(1 - \frac{\alpha \ln(R/s)}{St}\right)^{1/2}. \quad (4.7)$$

Close to the bouncing transition, when St is only slightly larger than St_c , the coefficient of restitution is close to zero and can be approximated by

$$\epsilon \simeq \frac{(St - St_c)^{1/2} [St - \alpha \ln(R/s)]^{1/2}}{St_c}. \quad (4.8)$$

If one of the two dissipative processes can be neglected, the above expression can be simplified and lead to different scaling laws. Indeed, when $St_{ic} \ll \alpha \ln(R/s)$ the global coefficient of restitution reduces to $\epsilon \simeq St/St_c - 1$ close to St_c , whereas it reduces to $\epsilon \simeq (St/St_c - 1)^{1/2}$ when $St_{ic} \gg \alpha \ln(R/s)$.

The coefficient of restitution of the global collision process ϵ predicted by eq. (4.5) is plotted as a function of the global Stokes number St in figure 7. In fig. 7(a), the relative shift lengths s/R are varied keeping $St_{ic}=0$, so that the critical Stokes number St_c varies according to eq.(3.10), and the $\epsilon(St)$ curve changes accordingly, but only with a global shift by keeping the same shape. Note that the set of curves of figure 7(a) is very similar to the set of $\epsilon(St)$ curves shown by Izard, Bonometti & Lacaze (2014) for different relative sphere roughnesses. When the dissipation during the solid collision is taken into account in figure 7(b) at a constant $s/R = 10^{-2}$, the critical Stokes number increases with increasing dissipation so that the $\epsilon(St)$ curve changes accordingly, here with no global shift but with a shape deformation. The two separate dissipation processes arising

in the approach phase and in the solid contact have thus a very distinct influence on the $\epsilon(St)$ curve.

In figure 8(a), the global coefficient of restitution ϵ is now plotted as a function of the global Stokes number St for the experimental data together with the model equations corresponding to three different St_c values: $St_c = 4, 5$ and 6 . As the experimental data are very close to the bouncing transition, the theoretical curves are very close to straight lines of equation $\epsilon = St/St_c - 1$ for $St/St_c \geq 1$. The experimental data for which a rebound is observed ($\epsilon > 0$) are within the band delimited by the two curves drawn for $St_c = 4$ and 6 as we have already shown that $4.5 \lesssim St_c \lesssim 6$ when bouncing is observed (figure 6b).

Finally, ϵ is plotted in figure 8(b) as a function of the reduced Stokes number St/St_c . The experimental data are in the quite narrow range $0.6 \lesssim St/St_c \lesssim 1.1$ around the critical transition value $St/St_c = 1$. It is very satisfying that the data without bouncing ($\epsilon = 0$) are observed to fall such as $St/St_c < 1$, and that the data with bouncing ($\epsilon > 0$) are quite close to the theoretical master curve of equation $\epsilon = St/St_c - 1$ for $St/St_c \geq 1$. The bouncing transition is abrupt with a linear increase of ϵ with St just above St_c .

5. Conclusion

The normal impact of a liquid-immersed sphere on a micro-textured wall has been analyzed taking into account the influence of viscous dissipation on the hydrodynamic and solid contact interactions between the sphere and the textured wall. The wall texture consists of an array of square micro-pillars. In our previous works, the separate effect of the texture geometrical parameters on the elastic contact force (Chastel, Gondret & Mongruel 2016) and lubrication drag (Chastel & Mongruel 2019) had been assessed independently. Here, these effects are combined to yield a complete description of the collision process. An equation of motion for the sphere is proposed, describing its whole dynamics, that comprises the approach to the wall, the contact with the wall and also the subsequent rebound. As the wall textures reduces the lubrication pressure, the pillar deformation considered in the model does not result from the fluid pressure but from the solid contact force that arises when the sphere touches the top of the textures with a non-zero impact velocity. Experimental data previously obtained by high-frequency interferometry can be now entirely described by the modeling with a good agreement.

An analytical expression is derived for the critical Stokes number for bouncing, St_c , that arises from the sum of two contributions corresponding to dissipation prior and during the contact. Both contributions are strongly influenced by the geometrical parameters of the wall texture and the predictions are in agreement with the experimental data. An analytical expression is also derived for the coefficient of restitution ϵ as a function of the Stokes number St . The predicted linear evolution of ϵ with $St - St_c$ just above St_c is in found in good agreement with the experimental measurements.

The theoretical modeling developed in the present paper is for viscous fluids, i.e. when viscous dissipation from the interstitial fluid flow is much larger than all the other possible dissipation sources such as the viscoelasticity or plasticity of the solid materials or the excitation of vibrational modes.

These findings are useful to understand precisely the influence of a surface roughness on the viscous dissipation in the near-wall bouncing dynamics. The methodology presented here could be extended to other surface roughness geometries. The present findings may also be useful for the implementation of realistic collisional models in numerical methods to simulate the flow of suspensions and liquid-immersed granular flows as in Biegert,

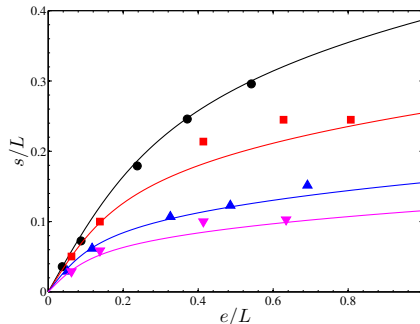


FIGURE 9. Evolution of the near-field shift length s normalized by the periodic spacing of the pillars L as a function of the normalized height of the pillars e/L . Data symbols correspond to the experimental values from Chastel & Mongruel (2019) for $\phi = 0.05$ (\bullet), 0.15 (\blacksquare), 0.30 (\blacktriangle), and 0.45 (\blacktriangledown), and the solid lines correspond to eq. (A4) without any fitting parameters.

Vowinckel & Meiburg (2017).

The authors wish to thank T. Chastel for measurements, A. Phor for data processing, and J. Magnaudet for fruitful discussions. Suggestions from the referees are gratefully acknowledged.

The authors report no conflict of interest.

Appendix A. Dependence of the near-field shift length s upon the geometrical parameters of the textured wall

The near-field ($h \ll L$) shift length s used throughout the modeling has been measured by Chastel & Mongruel (2019). Figure 9 illustrates how this parameter depends on the geometrical parameters of the pillar arrays. For a given value of pillar fraction ϕ , the dimensionless shift length s/L increases with dimensionless pillar height e/L . Smaller pillar fractions ϕ result in larger shift length values. In the following, we propose a correlation between s/L , e/L and ϕ , that is based on simple scaling arguments. First, in the limit of small pillar height ($e/L \ll 1$), far-field and near-field shift lengths must coincide, which yields a linear dependence with pillar height, with a slope increasing with decreasing ϕ (Chastel & Mongruel 2019):

$$\frac{s}{L} = (1 - \phi) \frac{e}{L}. \quad (\text{A1})$$

In the limit of large pillar heights ($e/L \approx 1$), the viscous dissipation on the pillar lateral walls has to be taken into account. This can be done through a bilayer model (Seiwert, Clanet & Quéré 2011), in which the pillars and fluid around them are considered as a continuum of effective viscosity $\eta_{eff} = k\eta$, where k is a dimensionless coefficient that depends on the geometrical parameters (e/L and ϕ) of the pillar array:

$$k = \frac{\eta_{eff}}{\eta} = 1 + \beta(\phi) \left(\frac{e}{L}\right)^2 \simeq \beta(\phi) \left(\frac{e}{L}\right)^2. \quad (\text{A2})$$

In the above equation, the coefficient $\beta(\phi)$ is related to the drag per unit length on a pillar in the array of pillars. This coefficient is an increasing function of ϕ which can be calculated by an analytical formula from Kuwabara (1959): $\beta = 13.8, 36.2,$

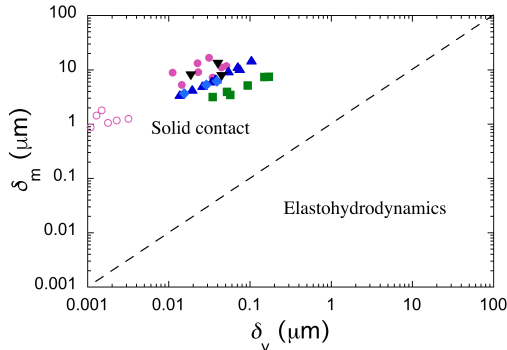


FIGURE 10. Measured sphere penetration depth δ_m as a function of the estimated elastohydrodynamic deformation of pillars δ_v for all the experiments (data symbols of table 1 with filled (open) symbols for (non) bouncing case), together with the line of equation $\delta_m = \delta_v$ (- -) delineating the domain of elastohydrodynamic deformation from the domain of deformation by solid contact.

90.3, 107 for $\phi = 0.05, 0.15, 0.30, 0.45$, respectively. In the bilayer model of Chastel & Mongruel (2016), the radial pressure gradient in the squeeze flow between the sphere and the top of the pillars is found to have a similar form as in classical lubrication theory: $dp(r)/dr = -6\eta r V(h)/\bar{h}(r)$, where $\bar{h}(r)$ is a function of e, k and $h + r^2/eR$. Thus, $\bar{h}(r)$ is a characteristic distance that yields the shift length as $s = \lim_{h \rightarrow 0} \bar{h} = e/k^{1/3}$, leading to the scaling law

$$\frac{s}{L} \sim \left(\frac{e}{\beta(\phi)L} \right)^{1/3}. \quad (\text{A3})$$

An equation model based on the two limiting behaviours (A1) and (A3) can be built as :

$$\frac{s}{L} \simeq (1 - \phi) \left(\frac{e}{L} \right) \left[1 + \beta(\phi) \left(\frac{e}{L} \right)^2 \right]^{-1/3}. \quad (\text{A4})$$

It can be seen in figure 9 that the experimental values of s are quite well described by eq. (A4) over the whole range of geometrical parameters of the textures considered here.

Appendix B. On the possible elastohydrodynamic deformation

In this appendix, we look at the possible elastohydrodynamic deformation. The lubrication force exerted on the sphere during its approach close to the wall textures is $F_D = -6\pi R^2 \eta V(h)/(h + s)$. This effective viscous force, which stems from the interaction of the sphere with the texture, results from an effective local pressure $p(h, r) = -3R\eta V(h)/(h + r^2/2R + s)^2$ that may lead to a possible deformation of the pillars. The maximum elastic deformation δ_v that would result from the maximal pressure $p(0, 0)$ is

$$\delta_v \simeq \frac{e}{E} p(0, 0) \simeq \frac{3\eta e R V_i}{E s^2}. \quad (\text{B1})$$

In the experiments considered here, this elastohydrodynamic deformation δ_v would be typically between about 0.001 and 0.1 μm , which is smaller or of the order of the microscopic roughness ξ of the sphere surface and texture surface. Such an elastohydrodynamic deformation may thus be neglected and solid contact may be considered to happen at

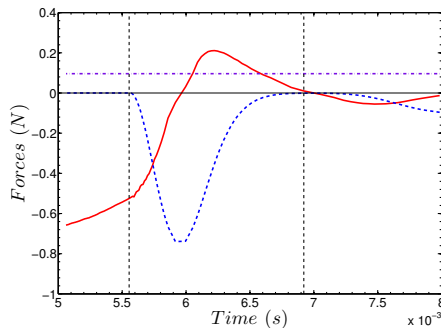


FIGURE 11. Model forces as a function of time for the case of fig. 3b with $2R = 14$ mm, $\phi = 0.05$, $2b = 56$ μm , and $e = 57$ μm . Viscous drag force F_D (—), solid contact force F_w (- - -), and apparent weight $F_g + F_A$ (- · - ·) of the immersed sphere. The two vertical dotted lines indicate the times of initial and final solid contact.

$h = 0$. When neglecting gravity and any fluid effects, the elastic deformation from solid contact has been shown by CGM 2016 to be

$$\delta_{m0} = \left(\frac{2\rho_s e R^2 V_i^2}{\phi E} \right)^{1/3}. \quad (\text{B2})$$

The ratio of the two elastic deformations from either viscous or solid interaction is thus

$$\frac{\delta_v}{\delta_{m0}} \simeq \frac{3\eta}{s^2} \left(\frac{\phi e^2 R V_i}{2\rho_s E^2} \right)^{1/3}. \quad (\text{B3})$$

In the experiments considered here, this ratio is in the range $0.001 \lesssim \delta_v/\delta_{m0} \lesssim 0.02$ meaning that the elastohydrodynamic deformation is negligible when compared to the elastic deformation from solid contact. In the plot of fig. 10 where the measured deformation δ_m is displayed as a function of the estimated elastohydrodynamic deformation δ_v , one clearly see that all the data points are well above the line $\delta_m = \delta_v$, thus in the domain of solid contact and not in the domain of elastohydrodynamics.

All the length scales embedded in the problem can be sorted as follows relative to the spatial resolution of the measurements $\Delta \simeq 0.2\mu\text{m}$:

$$\delta_v \lesssim \xi < \Delta \ll \delta_m \ll s(e, b, L) \ll R.$$

Appendix C. Time evolution of the difference force terms acting during the approach and collision of the sphere with the wall

We look here at the time evolution of the different forces and their relative importance when the sphere is approaching and colliding with the wall. An example of such force evolution is shown in figure 11 for the case of fig. 3b where the sphere bouncing is just small enough so that the sphere does not bounce off the wall. It thus corresponds to the data point where $\epsilon = 0$ at $St = St_c$ in figure 8b. Before solid collision ($t \lesssim 5.5 \times 10^{-3}$ s), the lubrication force $|F_D|$ is much larger than the apparent weight $|F_g + F_A|$, so that the sphere velocity decreases strongly. At the solid collision, the contact force $|F_w|$ increases strongly and reaches its maximum at $t \simeq 6 \times 10^{-3}$ s, corresponding to the maximal penetration distance of the sphere where the sphere velocity is zero and the viscous drag

is thus also zero. In the particular case of fig. 11 corresponding to the critical Stokes number where the “rebound” of the sphere is just $h = 0$ at $t \simeq 7 \times 10^{-3}$ s, the sphere then reaches its final static value for which the contact force just balances the apparent weight at $t \simeq 8 \times 10^{-3}$ s.

REFERENCES

- ARDEKANI, A. M & RANGEL, R. H. 2008 Numerical investigation of particle–particle and particle–wall collisions in a viscous fluid. *J. Fluid Mech.* **596**, 437–466.
- BARNOKY, G. & DAVIS, R. H. 1988 Elastohydrodynamic collision and rebound of spheres: Experimental verification. *Phys. Fluids* **31**, 1324–1329.
- BIEGERT, E., VOWINCKEL, B. & MEIBURG, E. 2017 A collision model for grain-resolving simulations of flows over dense, mobile, polydisperse granular sediment beds. *J. Comp. Phys.* **340**, 105–127.
- BIRWA, S. K., RAJALAKSHMI G., GOVINDARAJAN, R. & MENON, N. 2018 Solid-on-solid contact in a sphere-wall collision in a viscous fluid. *Phys. Rev. Fluids* **3**, 044302.
- CAWTHORN, C. J. & BALMFORTH, N. J. 2010 Contact in a viscous fluid. Part 1. A falling wedge. *J. Fluid Mech.* **646**, 327–338.
- CHASTEL, T. 2015 Interactions hydrodynamiques entre une sphère et une paroi texturée : approche, collision et rebond. *PhD thesis*, Université Pierre et Marie Curie.
- CHASTEL, T. & MONGRUEL, A. 2016 Squeeze flow between a sphere and a textured wall. *Phys. Fluids* **28** 023301.
- CHASTEL, T., GONDRET, P. & MONGRUEL, A. 2016 Texture-driven elastohydrodynamic bouncing. *J. Fluid Mech.* **805**, 577–590.
- CHASTEL, T. & MONGRUEL, A. 2019 Sticking collision between a sphere and a textured wall in a viscous fluid. *Phys. Rev. Fluids* **4** 014301.
- COSTA, P., BOERSMA, B.J., WESTERWEEL, J. & BREUGEM, W.-P. 2015 Collision model for fully resolved simulations of flows laden with finite-size particles. *Phys. Rev. E* **92**, 053012.
- DAVIS, R. H., SERAYSSOL, J.-M. & HINCH, E. J. 1986 The elastohydrodynamic collision of two spheres. *J. Fluid Mech.* **163**, 479–497.
- FALCON, E., LAROCHE, C. FAUVE, S. & COSTE, C. 1998 Behavior of one inelastic ball bouncing repeatedly off the ground. *Eur. Phys. J. B* **3**, 45–57.
- GONDRET, P., LANCE, M. & PETIT, L. 2002 Bouncing motion of spherical particles in fluids. *Phys. Fluids* **14**, 643–652.
- HUNTER, S. C. 1957 Energy absorbed by elastic waves during impact. *J. Mech. Phys. Solids* **5**, 162–171.
- IZARD, E., BONOMETTI, T. & LACAZE, L. 2014 Modelling the dynamics of a sphere approaching and bouncing on a wall in a viscous fluid. *J. Fluid Mech.* **747**, 422–446.
- JOHNSON, K.L. 1985 Contact Mechanics., Cambridge University Press, Cambridge.
- JOSEPH, G. G., ZENIT, R., HUNT, M. L. & ROSENWINKEL, A. M. 2001 Particle wall collisions in a viscous fluid. *J. Fluid Mech.* **433**, 329–346.
- KING, H., WHITE, R., MAXWEL, I. & MENON, N. 2011 Inelastic impact of a sphere on a massive plane: Nonmonotonic velocity-dependence of the restitution coefficient. *EPL* **93**, 14002.
- KUWABARA, S. 1959 The forces experienced by randomly distributed parallel circular cylinders or spheres in a viscous flow at small Reynolds numbers. *J. Phys. Soc. Japan* **14**, 527–532.
- LECOQ, N., FEUILLEBOIS, F., ANTHORE, N., ANTHORE, R., BOSTEL, F. & PETIPAS, C. 1993 Precise measurement of particle-wall hydrodynamic interactions at low Reynolds number using laser interferometry. *Phys Fluids A* **5**, 3–12.
- LECOQ, N., ANTHORE, R., CICHOCKI, B., SZYMCAK P., & FEUILLEBOIS, F. 2004 Drag force on a sphere moving towards a corrugated wall *J. Fluid Mech.* **513**, 247–264.
- LEDESMA-ALONSO, R., RAPHAËL, E., LÉGER, L., RESTAGNO, F. & POULARD, C. 2016 Stress concentration in periodically rough Hertzian contact: Hertz to soft-flat-punch transition. *Proc. R. Soc. A* **472**, 20160235.
- LEGENDRE, D., ZENIT., R., DANIEL, C. & GUIRAUD, P. 2006 A note on the modelling of the bouncing of spherical drops or solid spheres on a wall in viscous fluid. *Chem. Eng. Sci.* **61**, 3543–3549.

- LIAN, G., ADAMS, M. J., & THORNTON, C. 1996 Elastohydrodynamic collisions of solid spheres. *J. Fluid Mech.* **311**, 141–152.
- MARSHALL, J. S. 2011 Viscous damping force during head-on collision of two spherical particles. *Phys. Fluids* **23**, 013305.
- MARUOKA, H. 2019 Intermediate asymptotics on dynamical impact of solid sphere on millitextured surface. *Phys. Rev. E* **100**, 053004.
- MILNE-THOMSON, L. M. 1968 *Theoretical Hydrodynamics*. Dover.
- MONGRUEL, A., LAMRIBEN, C., YAHIAOUI, S. & FEUILLEBOIS, F. 2010 The approach of a sphere to a wall at finite Reynolds number. *J. Fluid Mech.* **661**, 229–238.
- RUIZ-ANGULO, A., ROSHANKHAH, S., & HUNT, M.L. 2019 Surface deformation and rebound for normal single-particle collisions in a surrounding fluid. *J. Fluid Mech.* **871**, 1044–1066.
- SEIWERT, J., CLANET, C., & QUÉRÉ, D. 2011 Coating of a textured solid. *J. Fluid Mech.* **669**, 55–63.
- SIMEONOV, J.A. & CALANTONI, J. 2012 Modeling mechanical contact and lubrication in Direct Numerical Simulations of colliding particles. *Int. J. Multiphase Flow* **46**, 38–53.
- SMART, J.R. & LEIGHTON, D.T. 1989 Measurement of the hydrodynamic surface roughness of noncolloidal spheres. *Phys. Fluids A* **1**, 52–60.
- YANG, F.-L & HUNT, M. L.. 2008 A mixed contact model for an immersed collision between two solid surfaces. *Phil. Trans. R. Soc. A* **366**, 2205–2218.